Experimental characterization of an unsteady laminar separation bubble on a pitching wing

Grille Guerra, A.; Mertens, C.; Little, Jesse C.; van Oudheusden, B.W.

Experimental characterization of an unsteady laminar separation bubble on a pitching wing

Adrian Grille Guerra[1,2] · Christoph Mertens[2] · Jesse Little[1] · Bas van Oudheusden[2]

Abstract

The laminar separation bubble (LSB) that forms on the suction side of a modified NACA 64_3-618 airfoil at a chord-based Reynolds number of $Re = 200,000$ is studied using wind tunnel experiments. First, the LSB is characterized over a range of static angles of attack, in terms of the locations of separation, transition and reattachment—using surface pressure measurements, particle image velocimetry (PIV) and infrared thermography (IT). For the conditions tested, excellent agreement between the techniques is obtained. Subsequently, a pitching motion is imposed on the wind tunnel model, with reduced frequencies up to $k = 0.25$. While surface pressure measurements and PIV are not affected by the change in experimental conditions, the infrared approach is impaired by the thermal response of the surface. To overcome this, an extension of the differential infrared thermography (DIT) method for detecting the three characteristics of an unsteady LSB is considered. All three experimental techniques indicate a hysteresis in bubble location between the pitch up and pitch down phases of the motion, caused by the effect of the aerodynamic unsteadiness on the adverse pressure gradient. However, the DIT measurements suggest a larger hysteresis, which is attributed to the thermal response time of the model surface. The experimental results measured with the pressure sensors reveal that the hysteresis in bubble location is larger than the hysteresis in lift, indicating that the observed bubble hysteresis is not purely due to instantaneous flow conditions, but has an inherent component as well.

List of symbols

α	Pitch angle [°]
$\dot{\alpha}$	Pitch rate [°/s]
α_m	Thermal diffusivity [m²/s]
ρ	Fluid density [kg/m³]
ρ_m	Material density [kg/m³]
a	Pitch axis position relative to mid-chord
Bi	Biot number
c	Airfoil chord length [m]
c_ℓ	Lift coefficient
c_p	Pressure coefficient
C	Theodorsen's function
C_m	Material heat capacity [J/(kg K)]
C_P	Fluid heat capacity [J/(kg K)]
f	Frequency [Hz]
Fo	Fourier number
h	Convective heat transfer coefficient [W/(m² K)]
k	Reduced frequency
k_m	Thermal conductivity [W/(m K)]
L	Penetration depth [m]
q_{irr}	Irradiation heat flux [W/m²]
q_∞	Freestream dynamic pressure [Pa]
Re	Reynolds number
St	Stanton number
t	Time [s]
t_c	Characteristic time scale [s]
T_∞	Ambient temperature [K]
T_c	Characteristic temperature scale [K]
T_s	Surface temperature [K]
U_∞	Freestream velocity [m/s]
x	Chordwise direction [m]

✉ Adrian Grille Guerra
a.grilleguerra@tudelft.nl

Christoph Mertens
C.Mertens@tudelft.nl

Jesse Little
jesselittle@arizona.edu

Bas van Oudheusden
B.W.vanOudheusden@tudelft.nl

[1] Department of Aerospace and Mechanical Engineering, The University of Arizona, 1130 N Mountain Ave, Tucson, AZ 85721, USA

[2] Faculty of Aerospace Engineering, Delft University of Technology, Kluyverweg 1, 2629 HS Delft, The Netherlands

y   Vertical direction [m]

z   Spanwise direction [m]

1 Introduction

At low Reynolds numbers, the boundary layer on the suction side of an airfoil may remain laminar into the adverse pressure gradient region, and separate forming a laminar shear layer. As the separated shear layer is strongly unstable it rapidly undergoes a transition-to-turbulence process. Under certain circumstances (Yarusevych et al. 2009), the turbulent shear layer may reattach to the surface and further develop as a turbulent boundary layer. This constitutes a region of the flow that is enclosed by the shear layer, that is referred to as a laminar separation bubble (LSB). Gaster (1967) and Horton (1968) were among the first to study steady LSBs, and characterized them, in the mean sense, using the three features described above: laminar separation, transition to turbulence and turbulent reattachment. Flow separation, and in particular the presence of a LSB, has detrimental effects on aerodynamic performance, reducing lift and increasing drag and noise emissions. The study of LSBs is thus relevant for the design of several devices that operate at chord-based Reynolds numbers (Re) in the order of Re $\sim O(10^4 - 10^5)$, as, for example, gliders, micro-air vehicles (Mueller and DeLaurier 2003), small-scale wind turbines (Giguère and Selig 1997) or low-pressure turbomachinery (Hodson and Howell 2005). Following the classic definition, the time-averaged topology of a steady LSB is illustrated in Fig. 1. Here, laminar separation and turbulent reattachment are found at the intersection of the surface with the mean dividing streamline that encloses the bubble from the outer flow. The transition process in the separated shear layer is of
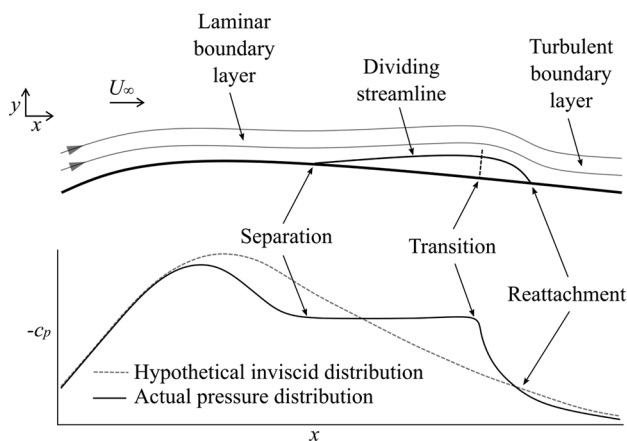

Fig. 1 Top: time-averaged topology of a LSB following the description of Horton (1968). Bottom: static pressure distribution with and without the presence of the LSB

particular interest for both basic and applied research purposes. Although this occurs over a region of finite extent, it is often simplified to a point for characterization purposes. The experiments of Watmuff (1999) and Lang et al. (2004), among others, have shown that amplification of the Kelvin–Helmholtz instability (Dovgal et al. 1994) in the shear layer is a common feature of LSBs, leading to the roll-up and shedding of spanwise coherent vortices at the rear part of the bubble. Simulations from Visbal et al. (2009), among others, showed that this effect compensates for the adverse pressure gradient, leading to a highly unsteady reattachment process associated with a turbulent boundary layer. Under particular circumstances, such as high turbulence levels or strong three-dimensionality, other instabilities can govern the transition process (Kurelek et al. 2020).

Extensive research has been done to study the influence of various parameters, such as Reynolds number (Burgmann and Schröder, 2008), angle of attack α (Yarusevych et al. 2009), freestream turbulence level (Balzer and Fasel, 2016; Hosseinverdi and Fasel, 2019) or three-dimensional effects (Toppings and Yarusevych, 2021) on the nature of LSBs. However, the study of LSBs under unsteady conditions is rather limited. This topic gains further relevance when considering gliders or unmanned aerial vehicles (UAVs), that are likely to operate in gusty environments such as close to the earth's surface (Reeh and Tropea, 2015; Guissart et al. 2021). The problem is aggravated by the recent shift toward composite manufacturing, which allow more efficient high-aspect-ratio configurations. When subjected to unsteady aerodynamic loads, composite wings will deform considerably more than traditional lower-aspect-ratio structures manufactured with conventional materials. Existing experiments on the characterization of unsteady LSBs (Pascazio et al. 1996; Lee and Basu, 1998; Kim and Chang, 2010) have mainly dealt with low-frequency pitching-type motions, observing a hysteresis in bubble location between the pitch up and pitch down parts of the cycle. This can be explained by means of the unsteady version of Bernoulli's equation, as discussed by Ericsson and Reding (1988). More recently, the experiments of Nati et al. (2015) and Guerra et al. (2021, 2022) have studied higher-frequency unsteady motions, representative of gust encounters or maneuvering situations for modern UAVs.

The experimental characterization of the unsteady behavior of a LSB under such conditions is more challenging than for steady situations, for which several flow measurement techniques have been successfully employed. These range from qualitative flow visualization to detect regions of separated flow, to more complex and quantitative analysis to determine the characteristic locations of the bubble: separation, transition and reattachment. Early studies, as, for example, the work of O'Meara and Mueller (1986), characterized steady LSBs at different angles

of attack from the static pressure distributions measured using pressure taps. The presence of the LSB makes the pressure distribution deviate from the inviscid solution, as illustrated in Fig. 1. Velocity measurements in the region of the bubble can be also used for characterization, using, for example, hot-wire anemometry (Watmuff, 1999), laser Doppler velocimetry (Lang et al. 2004) or particle image velocimetry (PIV) (Michelis et al. (2017); Kurelek et al. (2018)). Surface techniques, such as hot-film anemometry (Lee and Basu, 1998) or temperature-sensitive paint (TSP) (Miozzi et al. 2019), have also been explored for the study of LSBs, with the advantage of giving direct information at the aerodynamic surface of interest. In this regard, infrared thermography (IT) has gained recent attention for the detection of regions of separated flow (Dollinger et al. (2018)). As an optical technique, IT offers a higher spatial resolution than hot films, and is considerably more simple to operate than TSP as no painting of the surface is required. Modern infrared cameras, with improved thermal sensitivity and temporal resolution, allow tackling low-speed applications as is typically the case of a LSB (see, for example, the work of Wynnychuk and Yarusevych (2020)).

Not all of the flow measurement techniques mentioned above can be extended easily to unsteady conditions. For the case of unsteady LSBs, the most popular choice has been hot films (Rudmin et al. 2013) and PIV (Nati et al. 2015), but no comparison between the two has been reported. Regarding IT, unsteady regimes post an increased complexity due to the thermal response of the materials typically employed for aerodynamic surfaces. To overcome this limitation, Raffel and Merz (2014) proposed differential infrared thermography (DIT) for unsteady boundary layer transition detection. The working principle of the technique is to subtract two subsequently recorded infrared images and then identify the instantaneous transition region from the differential image. One of the goals of the present investigation is to extend the capabilities of the DIT method to characterize an unsteady LSB and set the basis for future exploration of different unsteady flow phenomena.

This study explores the unsteady behavior of an unsteady LSB that results from imposing a pitching-type motion onto a two-dimensional wing section. The topic is tackled using three different flow measurement techniques: surface pressure distributions, PIV and IT. The objective of the unsteady investigation is to measure the effect that the pitching dynamics have on the location of the bubble with the different measurement techniques. Based on this, a detailed assessment between the experimental techniques is provided, considering the results for the characterizations of both steady LSBs at different angles of attack, and unsteady LSBs at different levels of aerodynamic unsteadiness.

2 Experimental methods

2.1 Wind tunnel setup

The experiments were conducted in the Arizona Low Speed Wind Tunnel (ALSWT), situated in the Department of Aerospace and Mechanical Engineering at The University of Arizona. This closed loop facility has a test section of 0.91 m x 1.22 m x 3.66 m (height x width x length). The uniformity of the mean flow over the test section is at or better than 0.5 % and turbulence intensity is less than $Tu = 0.035\%$ in the range of 1 Hz to 10 kHz for the conditions considered here (Borgmann et al. 2020). The temperature inside the tunnel is regulated by a heat exchanger with a chilled water supply. Throughout the experiments, the temperature is held within the range of 0.55 °C of 22.2 °C. A pitot-static tube is mounted 0.4 m downstream of the test section entry at the tunnel side wall reaching into the freestream to acquire total and static pressures to determine the flow speed and as a reference for the static pressure measurements.

The wind tunnel model studied consists of a rectangular, quasi-two-dimensional wing formed using a modified NACA $64_3 - 618$ airfoil of the Aeromot 200 S Super Ximango motor glider, with a higher maximum lift coefficient than the original NACA $64_3 - 618$ (Guerra et al. 2021). The instrumented model is made out of carbon fiber and was constructed in-house at The University of Arizona. The chord length c is 304.8 mm, and the span is $4c$. The experiments are conducted at a freestream velocity U_∞ inside the test section of 10.8 m/s, which corresponds to a chord-based Reynolds number of Re = 200, 000. As discussed by Guerra et al. (2022), a LSB forms on the suction side of the wing at these conditions, covering approximately 25% of the chord.

To perform the investigation of the pitching airfoil, a VELMEX BiSlide stepping motor is connected to the wing spar at 40% of the chord using a wheel–crank mechanism. This can be used to change the angle of attack of the wing or to create a motion with constant pitching rate ($\dot{\alpha}$). The pitching rate can be adjusted by setting the *rpm* of the stepping motor. The motor is controlled using a VELMEX VXM-1 controller, which can simultaneously output a trigger signal at desired locations of the motion. This signal is used for phase-averaging of the static pressure measurements and triggering of the PIV system and infrared camera. The unsteady motion consists of pitching ramps of 10 degrees, between $\alpha = -3°$ and $\alpha = 7°$. Pitch up and pitch down ramps are studied separately, starting from quiescent conditions. In the experiments, the model is pitched between $\alpha = -4°$ and $\alpha = 8°$, to ensure that the traversing system accelerates from rest to the desired speed outside

Table 1 Test matrix of the pitching motions considered

		Quasi-steady				Unsteady			
Flow response	$\dot{\alpha}$ [°/s]	0.05	1.13	2.27	11.33	22.67	34.00	45.32	56.65
	f [Hz]	0.002	0.057	0.114	0.569	1.138	1.707	2.277	2.846
	k	~ 0.0002	0.005	0.010	0.050	0.100	0.150	0.200	0.250

		Quasi-steady	Unsteady						
Thermal response	Fo	~ 2300	80.7	40.4	8.1	4.0	2.7	2.0	1.6
	$Fo\,Bi$	~ 50	1.61	0.81	0.16	0.08	0.05	0.04	0.03

of the range of interest, which was verified by tracking the position of the wing in the raw PIV images. At $\alpha = 2°$ (middle of the motion), the aerodynamic pitching moment is zero at the location of the pitching axis. This creates a symmetric motion around that point and minimizes the aerodynamic loading on the pitching mechanism. Various pitching rates have been tested varying from a quasi-steady situation to a fully unsteady case, as listed in Table 1. For similarity with sinusoidal pitching motions available in the literature, an equivalent motion period is defined as double the time it takes to travel the full pitching ramp. From this, a reduced frequency k is defined, as $k = \frac{\pi f c}{U_\infty}$, where f is the inverse of the period.

The distinction between the quasi-steady ($k \leq 0.05$) and unsteady ($k > 0.05$) flow regimes is based on the definition proposed by Leishman (2006). It may serve to describe the aerodynamic response of the wing but is insufficient to completely characterize the influence of the unsteady motion on the IT measurements. These will also be affected by the thermal properties of the surface, in this case a carbon–fiber-–epoxy combination. The thermal response of a material is typically evaluated through a Fourier number Fo, defined as $Fo = \frac{\alpha_m}{fL^2}$, where α_m is the thermal diffusivity of the material and L the penetration depth. For the material employed in the present investigation, estimated values for these properties are given by Gardner et al. (2017). Apart from the material properties, temperature changes at the aerodynamic surface will depend on the convective heat transfer (h) with the flow. The relative importance of convective heat transfer may be expressed in terms of a Biot number, defined as $Bi = \frac{hL}{k_m}$, where k_m is the thermal conductivity of the material. A detailed description of the importance of these non-dimensional groups for unsteady IT measurements will be given in Sect. 2.5, where it will be shown that a quasi-steady thermal response requires that the product of Fo and Bi should be large with respect to unity.

The experimental setup is illustrated in Fig. 2. Detailed descriptions of the surface pressure, PIV and infrared measurement systems are given in the following.

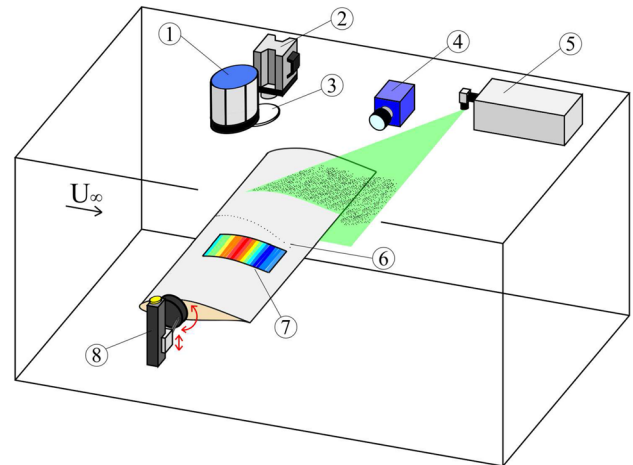## 2.2 Surface pressure measurements

Fig. 2 Sketch of the experimental setup. 1-Halogen lamp; 2-Infrared camera; 3-Ceiling aperture for infrared access; 4-PIV camera; 5-Laser head; 6-Mid-span pressure taps; 7-Region of interest for IT; 8-Pitching mechanism
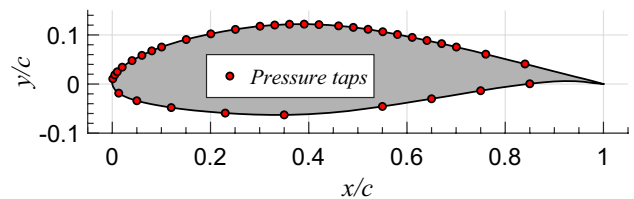

Fig. 3 Distribution of pressure taps along the chord at mid-span

The airfoil model contains 60 pressure taps for static pressure measurements. 36 of those are located along the chord at mid-span, as shown in Fig. 3, whereas the remaining 24 are located at 1/4 and 3/4 of the span, to assess the three-dimensionality of the flow. For the range of angles of attack investigated, a two-dimensional behavior was consistently observed, and therefore, only the results at mid-span will be discussed here. Scanivalve ZOC33 pressure scanners in combination with an ERAD Remote A/D module with a range of 2490 Pa are used to record static pressure. The

system is sampled at 504 Hz, during 10 s for static situations and 200 s for pitching investigations.

Phase-averaging of the data for the pitching airfoil is accomplished by simultaneously acquiring a trigger signal from the stepping motor controller that is sent at $\Delta\alpha = 1°$ increments. The accuracy of the system is given as $\pm 0.1\%$ of the measurement range. The uncertainty of the pressure measurements is estimated (with a 95% confidence interval, and following the description of Moffat (1988)) to be less than 4% of the freestream dynamic pressure (q_∞) for static configurations, while this value increases up to 7% for pitching situations. Uncertainty representation is omitted in the static pressure distribution results for clarity. For the unsteady case, the damping of the pressure tubing was considered by implementing a correction term extracted from the theoretical model of Bergh and Tijdeman (1965). However, no considerable effect could be appreciated, as a result of the low motion frequencies considered here (always below 3 Hz) and the fact that the pressure tubing was kept as short as possible (below 1 m length).

The characteristic locations of the LSB are extracted from the static pressure coefficient (c_p) distributions following the description of O'Meara and Mueller (1986), as illustrated in Fig. 4 from a static experimental setpoint. Flow separation causes the formation of a pressure plateau, which ends when transition to turbulence occurs. This is followed by a quick pressure recovery, linked to the reattachment process, after which the curve aligns again with the inviscid solution. In a wind tunnel experiment, the discrete distribution of pressure taps complicates the accurate determination of the location of these features. To overcome this spatial resolution limitation, some studies have proposed data fitting techniques to detect the characteristic locations of the bubble. For example, Gerakopulos et al. (2010) used a shape-preserving polynomial, whereas Boutilier and Yarusevych (2012) relied solely on linear fits. The approach considered here is to approximate the experimental data using four different linear fits between the onset of the adverse pressure

gradient and the trailing edge and estimate the characteristic locations of the LSB at the intersection of these.

2.3 Particle image velocimetry measurements

Planar PIV measurements are performed to analyze the evolution of the LSB on the suction side of the airfoil based on the flow topology. Submicron seeding particles (Di-Ethyl-Hexyl-Sebacate, DEHS) were introduced in the flow and illuminated with a Quantel Evergreen dual head laser. Images were acquired, in double-frame mode, with a LaVision Imager sCMOS camera. The camera had to be slightly tilted for optical access and was therefore equipped with a Scheimpflug adapter to maintain the full field of view in focus. The processing of the images was performed with the LaVision DaVis 8.3 software. All raw images were pre-processed using a temporal sliding minimum subtraction in order to increase the evaluation quality in the near-wall region, which is influenced by the laser-light reflections at the model surface. The main processing stage consisted of a multi-pass cross-correlation algorithm. The uncertainty of the mean velocity magnitude was estimated following the description of Wieneke (2017) and is given as a percentage of the freestream speed using a 95% confidence interval in Table 2. For the static characterization of the LSB, 800 images were acquired at 14 Hz for time-averaging. For the 400 phase-locked PIV images that were acquired for the pitching investigation, a programmable timing unit from the LaVision system was coupled with the trigger signal from the stepping motor controller. The main parameters of the PIV setup are summarized in Table 2.

The two-dimensional velocity fields obtained from planar PIV can be used to identify the dividing streamline (see Fig. 1) that encloses the bubble from the outer flow, thus enabling to estimate the locations of laminar separation and turbulent reattachment from its intersection with the surface (Kurelek et al. 2020). An estimation of the transition location may be obtained from turbulence statistics in the shear
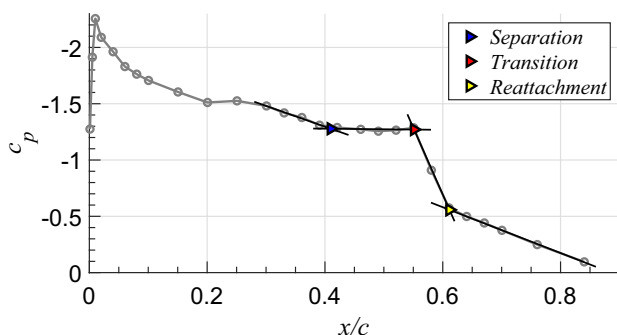

Fig. 4 Estimation of LSB characteristic locations from surface pressure distributions using linear fits

Table 2 PIV parameters

	Static	Unsteady
Number of images	800	400
Sampling rate	14 Hz	phase-locked
Laser pulse delay	30 μs	
Lens focal length	50 mm	
$f_\#$	4	
Sensor resolution	2560 $\times$ 2160 px	
Final pass window size	16 $\times$ 16 px	
Final pass overlap	75%	
Vector pitch	0.25 mm ($8.2 \times 10^{-4} \cdot c$)	
Velocity uncertainty	<2% U_∞	<5% U_∞

layer (Burgmann and Schröder, 2008) or boundary layer parameters (Wynnychuk and Yarusevych, 2020). The latter

approach is considered in this study by obtaining the evolution of boundary layer shape factor inside the bubble, and estimating transition as the location where the shape factor achieves a maximum value (Michelis et al. 2017).

2.4 Infrared thermography measurements

The surface temperature on the suction side of the wing is measured using an infrared camera sensitive in the middle-wavelength infrared (MWIR) band. Different cameras were used for the steady case and for the pitching investigation. The camera specifications are similar, but the camera used for the unsteady investigation has a higher frame rate, whereas the camera used for the steady measurements has a better spatial resolution. An overview of the infrared camera specifications is shown in Table 3. The infrared cameras were not specifically temperature calibrated (Raffel and Merz, 2014) for this experiment. The factory calibration was used to achieve an approximate estimate of the global temperature of the heated surface, but in the image processing stage only the infrared intensity measured directly by the sensor was considered. For the small temperature changes considered here, the calibration is quasi-linear and therefore the intensity distribution resembles well that of the temperature. Please note that the integration times are different between the two cameras to comply with the factory-calibrated values.

The IT configuration is shown in Fig. 5. In the region of interest, a thin film with low thermal conductivity was added to the airfoil skin, to increase surface emissivity and reduce conduction effects at the surface and into the wing inner structure. The wing was heated externally using a 1 kW halogen lamp placed above the wind tunnel test section, to enhance the convective heat transfer between the surface and the flow. For infrared optical access, a small orifice was made in the acrylic ceiling.

For the static measurements, the wing surface was first heated to around 10 K above ambient in quiescent conditions, and the wind tunnel was then started with the
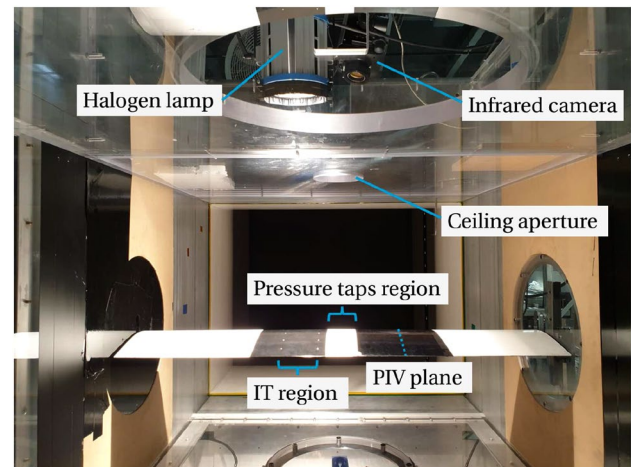

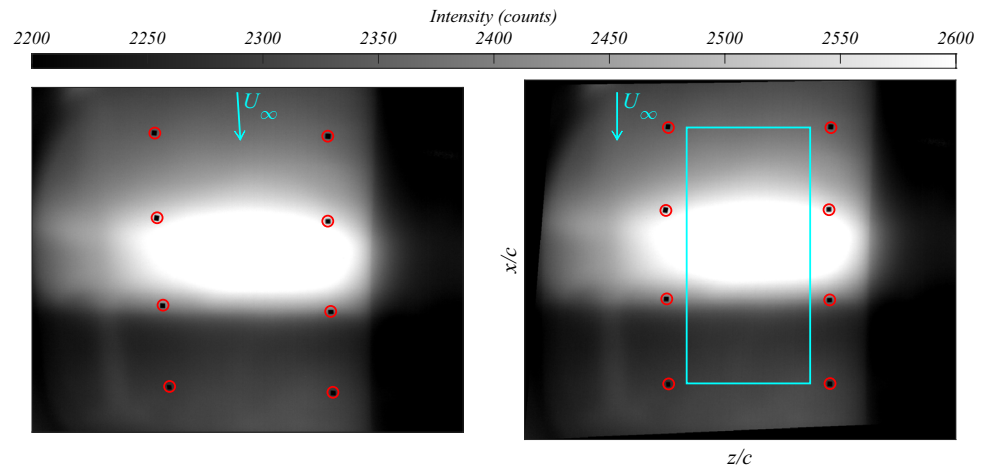**Fig. 5** Infrared thermography measurement setup in the wind tunnel

halogen lamp still turned on. When a steady-state temperature distribution was achieved (approximately 1 min after the wind tunnel speed settled), 500 images were sampled at 50 Hz for time-averaging. In the pitching investigation, pitch up and pitch down were studied separately. For a pitch up case, the wing was first moved to an angle of attack below the minimum of the motion of interest ($\alpha = 2° \pm 5°$) until a steady state was reached. The pitch up motion was then started, and the infrared camera was triggered by the stepping motor controller when α reached the beginning of the constant pitch ramp ($\alpha = -3°$). From there, the camera sampled at 180 Hz until $\alpha = 7°$ was reached. This way, the LSB is expected to move only in one direction during the acquisition (upstream for a pitch up case), simplifying the analysis of the thermal response of the surface. An analogous procedure was used to study the pitch down configuration.

The raw infrared images are dewarped by applying an image transformation constructed with the known location of copper tape fiducial markers on the wing. These appear as dark squares in the infrared images due to the low emissivity of the material. An example of a raw infrared image is shown in Fig. 6 left. The image in Fig. 6 right is obtained after applying a projective transformation based on the location of the eight markers. This image is now aligned with the flow in a coordinate system defined by the chord- and span-wise directions ($x - z$). The dewarped marker locations are also used to define a rectangular region of interest (shown in cyan). This region, centered between the two rows of markers, has a width of 25% of the airfoil chord, while it covers a chordwise extent of approximately 50% of the airfoil. The markers were placed such that the LSB is always located in this region. In the following, every infrared intensity distribution will be restricted to this region.

Table 3 IT parameters

	Static	Unsteady
Camera model	FLIR X8501sc	FLIR X6903sc
Spectral range	3–5 μm	3–5 μm
Thermal sensitivity (NETD)	<30 mK	<20 mK
Sampling rate	50 Hz	180 Hz
Number of images	500	Variable
Integration time	0.5 ms	2.8 ms
Lens focal length	50 mm	25 mm
Sensor resolution	1280 × 1024 px	640 × 512 px
$f_\#$	2.5	4

Fig. 6 Infrared images containing the detected markers for image dewarping. Left: Raw image. Right: Transformed image, showing the rectangular region of interest

2.5 Infrared thermography data analysis

The analysis of the infrared thermography measurements consists of relating the measured surface temperature distributions to the boundary layer state. The most common example is the detection of laminar-to-turbulent transition, by making use of the Reynolds analogy that links the momentum and thermal boundary layers White (2006). For the case of a LSB, this link is more complex, and derived from the direct numerical simulations of Spalart and Strelets (2000), which include the evolution of Stanton number (St) in the region of the bubble. The obtained trend is illustrated in Fig. 7. For the LSB at an incidence of α_1, St initially decreases as the laminar boundary layer gets thicker and continues to decrease in the initial portion of the bubble. The transition process in the separated shear layer induces near-wall velocity fluctuations and reverse flow, enhancing convection between the surface and the flow. The corresponding increase in heat transfer continues until reattachment, after which a gradual decrease is observed as the turbulent boundary layer gets thicker.

In order to detect the surface temperature changes that are caused by the variations in convective heat transfer, it is common practice in subsonic IT experiments to introduce an additional heat source that creates a temperature difference between the surface of interest and the flow. This can be achieved by switching off wind tunnel cooling (Gartenberg and Roberts, 1991), heating the model internally by Joule effect (Ricci and Montelpare, 2005), using electrically conductive paint coatings (Ghorbanishohrat and Johnson, 2018) or heating the model externally. The latter can be achieved by means ranging from simple halogen lamps (Grawunder et al. 2016), as considered in the present investigation, to more dedicated infrared heaters (Simon et al. 2016). For every situation, temperature changes should be kept small to prevent affecting the boundary layer state (Richter et al.
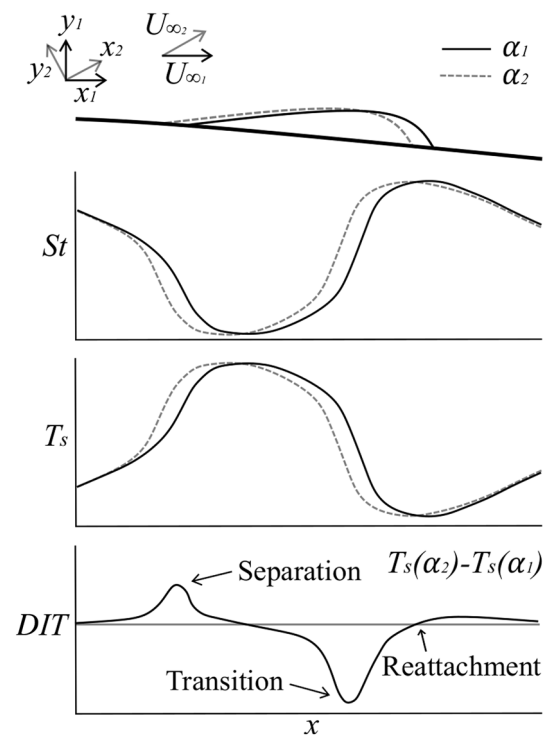

Fig. 7 From top to bottom: LSBs at incidences α_1 and α_2, Stanton number distributions, surface temperature distributions and differential infrared thermography distribution

2016). This also minimizes the effect of radiation exchange between the wind tunnel model and its environment.

Another key aspect of IT experiments is the choice of material properties for the model. In general, materials with low thermal conductivity are preferred, to avoid loss of spatial resolution due to a smearing effect. If the conditions are such that heat transfer by conduction and radiation may be neglected, and considering a wind tunnel model being heated externally, then the steady-state temperature distribution on the model is dictated by the balance between

convection to the flow and the incoming irradiation from the external source. For incompressible flows, Newton's law of cooling allows writing this as:

$$h(T_s - T_\infty) = q_{irr}, \tag{1}$$

where h is the convective heat transfer coefficient, T_s is the surface temperature of the model, T_∞ is the ambient temperature, and q_{irr} is the heat flux from the external source. For qualitative boundary layer diagnostics, as, for example, the characterization of a LSB, it is sufficient to link the surface temperature distribution that may be measured with an infrared camera to the evolution of the Stanton number. From its definition and Eq. (1), and assuming a constant level of the irradiation, a proportionality relation may be obtained as:

$$St = \frac{h}{U_\infty \rho C_P} \propto \frac{1}{T_s - T_\infty}, \tag{2}$$

where ρ and C_P are the fluid's density and heat capacity respectively. Based on this relation, the qualitative behavior of surface temperature for a case of a steady LSB is also illustrated in Fig. 7. Following this approach, Wynnychuk and Yarusevych (2020) were able to extract the three characteristic locations of a steady LSB using IT, in good agreement with PIV results.

Surface temperature typically does not only depend on the instantaneous convective heat transfer but also on the finite thermal responsiveness of the surface material itself (Wolf et al. 2020). To overcome the consequence of this limitation, Raffel and Merz (2014) proposed differential infrared thermography (DIT) as a technique for unsteady boundary layer transition detection. The principle of the technique is to subtract two subsequently recorded infrared images and then identify the instantaneous transition region from the differential image. It could be observed that, for a small time separation between images, the change in transition location due to the aerodynamic unsteadiness causes a visible temperature change, whereas no temperature changes occur for regions of the flow that remain mostly unchanged. The technique was first introduced for a pitching airfoil and compared to other experimental techniques by Richter et al. (2016) and later extended to study the unsteady transition phenomenon for a helicopter rotor in forward flight (Gardner et al. 2021). For the pitching airfoil case, the experiment was replicated using thermal simulations (Gardner et al. 2017) to investigate the effect of surface material properties or image time separation on the DIT results, among other parameters. This assessment showed that there is still a lag due to the thermal responsiveness of the surface, which causes an increasing error in the detected transition location for larger time separations between the subtracted images.

In this investigation, the capabilities of the DIT method will be extended to characterize an unsteady LSB. The proposed approach is illustrated in Fig. 7, by considering the bubble movement that would result from a small change in angle of attack, from α_1 to α_2. As discussed by Wolf et al. (2019), DIT provides information about the boundary layer state at the intermediate incidence $\frac{\alpha_1 + \alpha_2}{2}$. The DIT distribution given in Fig. 7 is obtained by subtracting the two surface temperature distributions, as $T_s(\alpha_2) - T_s(\alpha_1)$. As the LSB moves upstream from α_1 to α_2, the DIT curve shows a positive peak linked to the change in the laminar separation location, and a negative one linked to the transition process. Finally, reattachment is expected to occur where the DIT curve changes sign.

To explain the effect of the thermal response of the surface on the application of DIT, Eq. (1) is modified to account for an unsteady surface temperature evolution caused by a changing convective heat transfer. As a first approximation, it is assumed that the surface behaves as an ideal thermal insulator of thickness L, posting a similar thermal model to that considered by von Hoesslin et al. (2017, 2020). This may be expressed as:

$$\rho_m C_m L \frac{\partial T_s}{\partial t} = q_{irr} - h(T_s - T_\infty), \tag{3}$$

where ρ_m and C_m are the material density and heat capacity respectively. The thermal behavior of the system described by Eq. (3) can be conveniently characterized by considering the unsteady response of the surface temperature $T_s(t)$ to a sudden change in convective heat transfer, Δh. For this situation, integration of Eq. (3) in time yields:

$$T_s(t) - T_\infty = \frac{q_{irr}}{h(0) + \Delta h} + e^{-\frac{(h(0) + \Delta h)t}{\rho_m C_m L}} \left(T_s(0) - T_\infty - \frac{q_{irr}}{h(0) + \Delta h} \right). \tag{4}$$

A DIT signal, referred to as DIT, may be constructed as: $DIT = T_s(t) - T_s(0)$. For sufficiently small times, the exponential term in Eq. (4) may be linearized, which allows expressing the DIT signal as:

$$\frac{DIT}{T_S(0) - T_\infty} \approx -\frac{t \Delta h}{\rho_m C_m L}. \tag{5}$$

This non-dimensional expression gives a linear approximation to the behavior of the DIT method. After some manipulation, it can be further expressed in terms of other non-dimensional groups, as:

$$\frac{DIT}{T_c - T_\infty} \sim \frac{t_c \Delta h}{\rho_m C_m L} = \frac{k_m t_c}{\rho_m C_m L^2} \frac{\Delta h L}{k_m} = FoBi, \tag{6}$$

where T_c is the characteristic temperature of the surface and t_c is the characteristic time scale of the unsteady problem (for example, the period of a sinusoidal pitching motion). Here, Fo is a Fourier number and Bi is a Biot number, as defined in Sect. 2.1. The definition of the Biot number is now based

on a change in convective heat transfer, as, for example, the difference between laminar and turbulent regions when studying the unsteady transition process. For the conditions considered here, an estimation of this quantity may be obtained from the application of the Reynolds analogy to skin friction distributions obtained from XFoil simulations. This allows estimating the non-dimensional group Fo Bi that governs the unsteady thermal response of the surface, as listed in Table 1. This result highlights the importance of material properties for DIT. In general, materials with a low thermal capacity are preferred, which is in agreement with the simulations of Gardner et al. (2017). Besides, Eq. (6) is also affected by the change in convective heat transfer, which suggests that the application of DIT for unsteady LSB characterization may be challenging given the low levels of convection associated with low Reynolds number flows.

Fig. 8 LSB characteristic locations estimated from surface pressure distributions, for the wing at $\alpha = -3$, 2 and 7 degrees

3 Laminar separation bubble characterization

This section presents the results of the experimental characterization of the LSB in terms of its three characteristic locations for steady and unsteady conditions, based on the three different measurement techniques. While the performance of the selected approaches for the determination of these locations based on the surface pressure and the PIV measurements does not differ significantly between steady and unsteady conditions, the determination based on infrared thermography measurements is strongly impaired by the temperature response of the wing model surface in unsteady flow conditions. The analysis of the LSB hysteresis that is presented in this section following the characterization of the unsteady LSB is therefore performed based on the surface pressure measurements.

3.1 Steady LSB characterization

The characterization of the LSB is performed over a range of static angles of attack, between $-3° \leq \alpha \leq 7°$, in one-degree increments. The characteristic locations of the LSB are identified from the surface pressure measurements, the time-averaged flow fields obtained with PIV, and from the infrared thermography measurements.

The characterization of the LSB based on c_p distributions measured with surface pressure sensors is illustrated in Fig. 8 for $\alpha = -3°$, 2° and 7°. The results show an upstream shift of the bubble with increasing α, caused by a stronger adverse pressure gradient that is associated with the upstream shift and increase in magnitude of the pressure minimum. Apart from that, the results demonstrate the limitation of the technique for negative α for the present model, due to the poor resolution of pressure taps
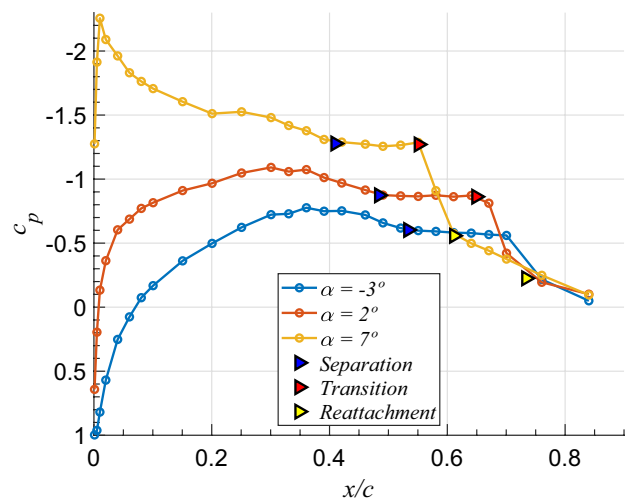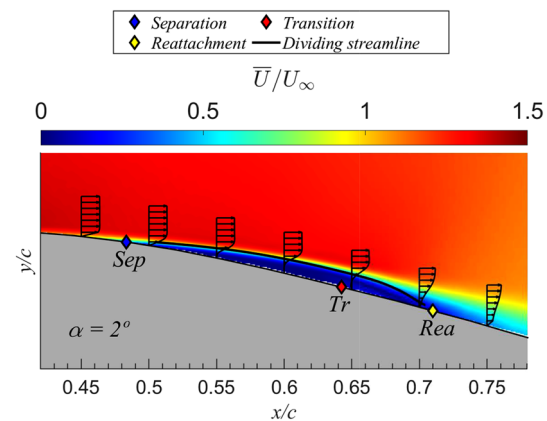

Fig. 9 Contours of time-averaged velocity magnitude from PIV measurements, for the wing at $\alpha = 2°$

closer to the trailing edge. This compromises the identification of transition and reattachment when these locations move too far downstream.

The flow topology of the LSB can be investigated in more detail using PIV. As an example, contours of time-averaged velocity magnitude are shown in Fig. 9 for the wing at $\alpha = 2°$, together with streamwise velocity boundary layer profiles at selected stations, as well as the characteristic LSB locations. The position of the bubble is identified with the mean dividing streamline that encloses the bubble from the outer flow at the airfoil's surface (Kurelek et al. 2018). The location of transition to turbulence, occurring in the separated shear layer, is estimated at the point where the boundary layer shape factor reaches a maximum inside the bubble (Wynnychuk and Yarusevych, 2020).

An example of the IT measurements is shown in terms of the time-averaged infrared radiation intensity measured on the suction side of the wing, for $\alpha = 2°$, which is shown in the top part of Fig. 10 left. A slightly nonhomogeneous distribution is observed along the span, caused by the inhomogeneous irradiation from the halogen lamp, but this does not interfere with the proper identification of the bubble. The LSB characteristic locations are extracted at each chordwise pixel row along the span. (Results are indicated by the black and white lines.) While a main advantage of the IT measurement technique is the possibility of measuring the spanwise behavior of the LSB, the observed trend in this particular case justifies the spanwise-averaging of the intensity distribution, as a means to reduce pixel noise. The obtained intensity distribution along the chord of the airfoil is shown on the bottom part of Fig. 10 left. The numerical gradient of the intensity curve is also indicated, to visualize the estimation of the LSB characteristic locations extracted from those curves. The measurements agrees well with the qualitative discussion extracted from Spalart and Strelets (2000) (see Fig. 7); the surface temperature (or infrared radiation intensity) is observed to increase in the laminar region, achieving a maximum in the upstream part of the bubble. The temperature then starts to decrease due to the effect of transition, which continues until it reaches a minimum when the turbulent boundary layer reattaches. Subsequently, the temperature starts to slowly increase again as the attached boundary layer develops.

The DIT method, developed to extend the capabilities of infrared imaging in unsteady regimes, can also be applied to static measurements (Wolf et al. 2019). For the first time, this method is applied here to study a LSB. The working principle of this approach is discussed in Sect. 2.5 and is illustrated in Fig. 7. The DIT distribution obtained when subtracting the static infrared intensity at $\alpha_1 = 1.5°$ from the one at $\alpha_2 = 2.5°$ is shown in Fig. 10 right. The LSB characteristic locations obtained from the spanwise-averaged curve represent the bubble at the intermediate value of α, this is, at $\alpha = \frac{\alpha_1 + \alpha_2}{2} = 2°$ (Richter et al. 2016). The separation between thermograms may be defined as $\Delta\alpha = \alpha_2 - \alpha_1 = 1°$. The obtained locations can be compared with those from the regular IT approach (Fig. 10 left), showing a discrepancy of less than 1% of the airfoil chord, and providing a proof of concept for the application of DIT to detect LSB characteristics.

The static IT and DIT approaches are further compared in Fig. 11, by showing spanwise-averaged distributions at $\alpha = -1$, 2 and 5 degrees. As in the example above, the DIT curves are constructed using a 1-degree difference in α between thermograms. This comparison shows again an
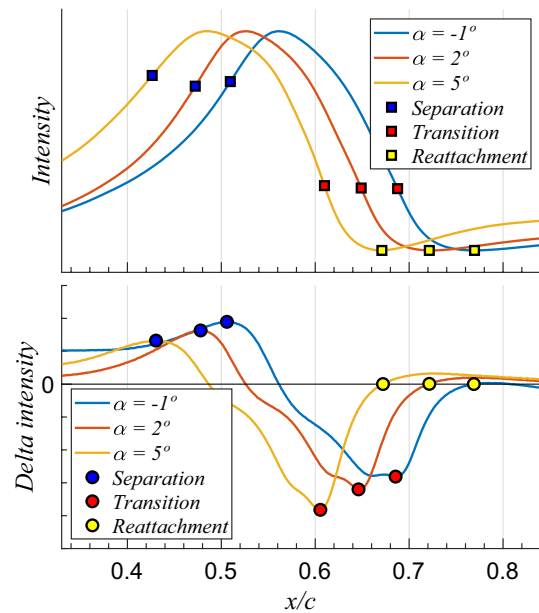

Fig. 11 LSB characteristic locations estimated from spanwise-averaged IT (top) and static DIT (bottom) distributions, for the wing at $\alpha = -1$, 2 and 5 degrees

Fig. 10 Left: Contours of time-averaged infrared intensity (top) and spanwise-averaged infrared intensity and intensity gradient distributions along the chord (bottom) for the wing at $\alpha = 2°$. Right: Contours of the difference in infrared intensity between $\alpha_1 = 1.5°$ and $\alpha_2 = 2.5°$ (top) and spanwise-averaged infrared intensity and DIT distributions along the chord (bottom)
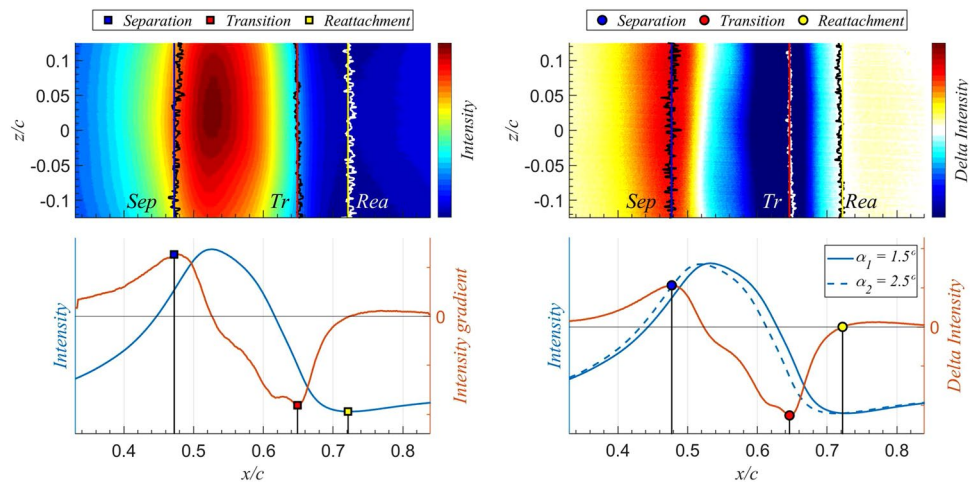
excellent agreement between the two infrared approaches for all three characteristic locations of the LSB.

The results for the characteristic LSB locations based on the three measurement techniques considered in this study (surface pressure measurements, PIV and infrared thermography) for every angle of attack considered, from $\alpha = -3°$ to $\alpha = 7°$, are shown in Fig. 12. From the infrared thermography measurements, only the results obtained with the DIT method are shown, as this was found to be analogous to the standard IT evaluation.

In general, all three techniques capture the upstream shift of the bubble with increasing incidence in good agreement with each other, showing deviations of less than 2% of the chord in the locations measured. As discussed earlier, some information is missing from the pressure taps in the negative incidence region due to the reduced density of taps toward the trailing edge of the wing. The main discrepancy appears in the detection of laminar separation from PIV for the range of moderate positive angles of attack. This can be attributed to the uncertainty in extrapolating the dividing streamline toward the surface, given the shallow shape of the bubble in this region (see Fig. 9).

3.2 Unsteady LSB characterization

The core of this study consists of the analysis of the unsteady LSB behavior when subjected to a pitching motion imposed to the wing. This consists of pitch up and pitch down ramps at a constant pitch rate, $\dot{\alpha}$, between $\alpha = -3°$ and $\alpha = 7°$, as described in Sect. 2.1. Different levels of unsteadiness are investigated, as listed in Table 1, by changing the pitch rate, to assess the impact on the bubble and also on the performance of the different experimental techniques.

A first visualization of the effect of the pitching motion on the LSB is presented in Fig. 13, where a comparison between the phase-averaged static pressure distributions at $\alpha = 2°$ during pitch up and pitch down is shown, for the pitching wing with $k = 0.15$. The measured pressure distributions differ significantly for this condition, and the characteristic locations of the LSB, which are obtained following the same methodology as for the static investigation, indicate a significant hysteresis in the LSB location between pitch up and pitch down, as the LSB occurs 5% of the chord further upstream during pitch down.

The LSB hysteresis between pitch up and pitch down is captured based on the surface pressure measurements over the full pitch angle range, as shown in Fig. 14 for one-degree increments in α at the pitch rate corresponding to $k = 0.15$. However, as for the static results discussed in Sect. 3.1, the method fails to detect transition and/or reattachment when the bubble moves close to the trailing edge, where fewer pressure taps are available. This limitation is consistent over the entire range of k that was measured with the pressure sensors.
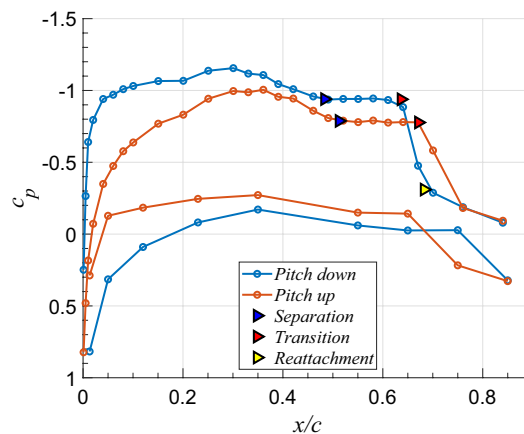
Fig. 13 Phase-averaged c_p distributions for the pitching wing at $\alpha = 2°$, both for pitch up and pitch down, with $k = 0.15$
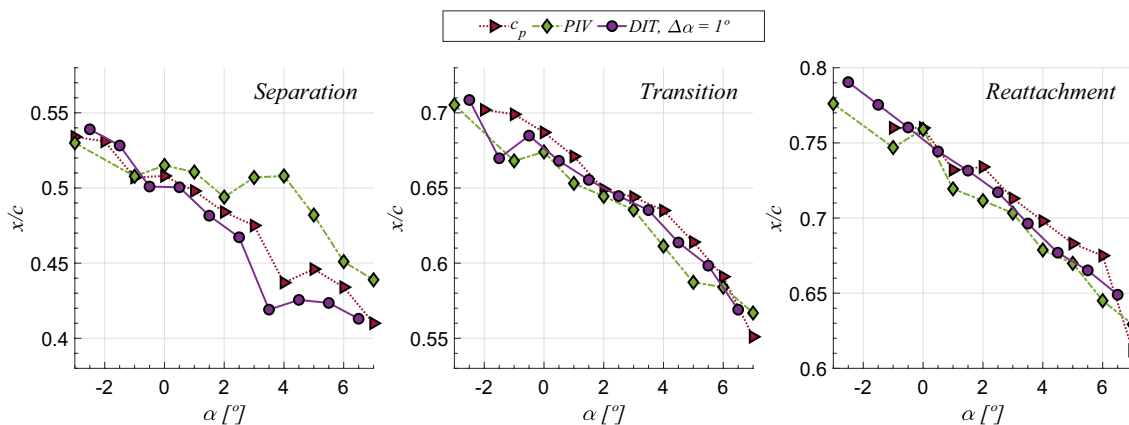
Fig. 12 Comparison of the LSB characteristic locations measured with three different flow measurement techniques, for the full range of static angles of attack considered, $-3° \leq \alpha \leq 7°$
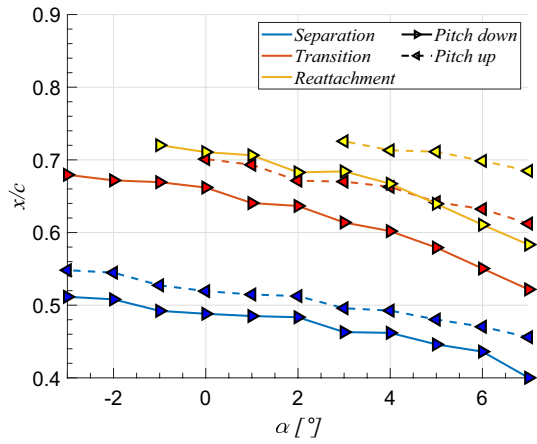
Fig. 14 LSB characteristic locations estimated from c_p distributions, for the full pitching ramps, both up and down, with $k = 0.15$
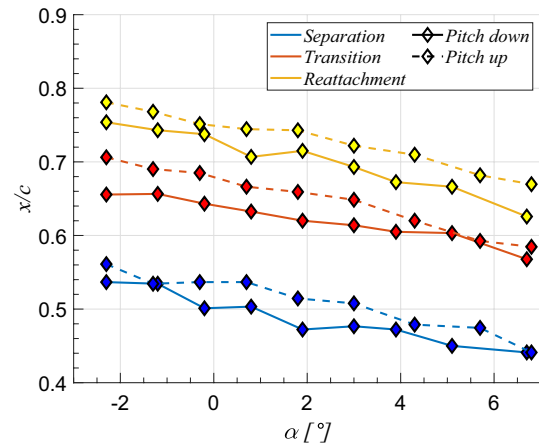
Fig. 16 LSB characteristic locations estimated from PIV, for the full pitching ramps, both up and down, with $k = 0.15$

From the PIV measurements, contours of the phase-averaged velocity magnitude, for $k = 0.05$ and $k = 0.15$, are shown in Fig. 15 left and Fig. 15 right, respectively, both for pitch up and pitch down at $\alpha = 2°$. The characteristic locations of the bubble are extracted similarly as for the static characterization, using the mean dividing streamline and the evolution of boundary layer shape factor.

Nine separate PIV measurements were conducted for each pitching ramp, and the instantaneous pitch angle was retrieved directly from the raw PIV images. As a consequence, the LSB characteristic locations can be determined over the entire range of α for both pitch up and pitch down, the results of which are shown for $k = 0.15$ in Fig. 16. In contrast to the characterization results based the surface pressure measurements, all three LSB characteristics are captured over the entire range of α with the PIV

measurements, which are, however, limited to two reduced frequencies ($k = 0.05$ and $k = 0.15$) in this study.

It is shown in Sect. 3.1 that DIT can in principle be applied to detect the three characteristic locations of the unsteady LSB. However, as discussed in Sect. 2.5, the application of DIT is linked to the thermal response of the aerodynamic surface. For the smallest reduced frequency considered, $k = 0.0002$, the LSB behavior basically follows the static characterization discussed in Sect. 3.1. Not only that, but also the instantaneous temperature distribution resembles that of the analogous static angle of attack. This holds when $\mathrm{Fo\,Bi} \gg 1$, which justifies the distinction between quasi-steady and unsteady motions based on the thermal response of the surface (see Table 1). The application of DIT to such a thermally quasi-steady motion is shown in Fig. 17, where DIT curves are constructed, centered at

Fig. 15 Phase-averaged velocity magnitude for the pitching wing at $\alpha = 2°$ during pitch up (bottom) and pitch down (top). Left: $k = 0.05$. Right: $k = 0.15$
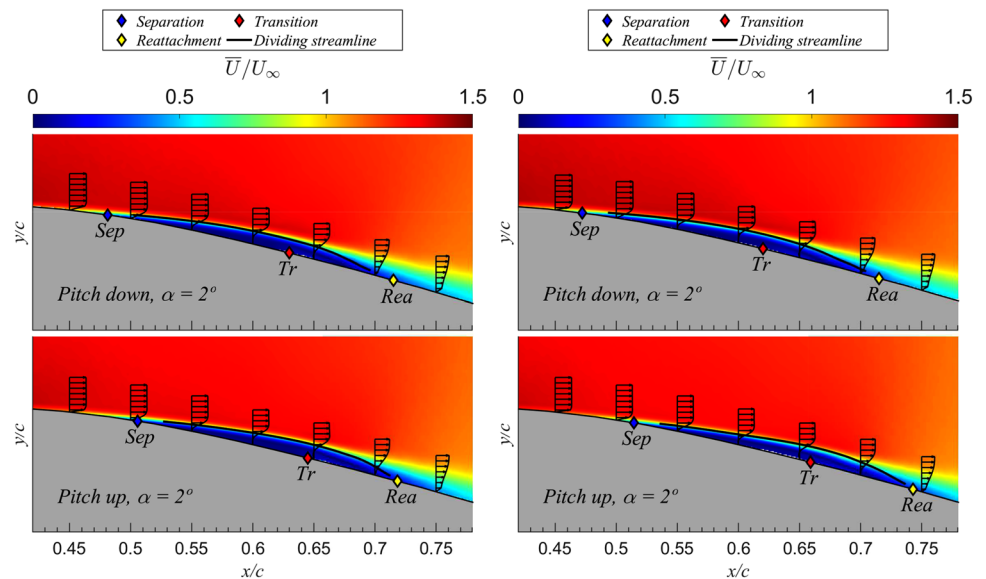
$\alpha = 2°$, using various separations between infrared frames, $\Delta\alpha$. The DIT peaks (positive for separation and negative for transition, as $\Delta\alpha > 0$) change in strength and location with the different DIT frame spacing considered. As discussed by Gardner et al. (2017) for unsteady transition on a pitching airfoil, increasing the time difference (or angle difference here) between the infrared frames used to construct the DIT curve causes an erroneous drift from the true location of interest, as indicated in Fig. 17 by including the characteristic locations measured with IT at $\alpha = 2°$. The preferred approach is therefore to minimize this difference, while the DIT peaks still remain detectable (Mertens et al. 2020). The obtained results also show a stronger peak for transition compared to separation (approximately double the strength), which could similarly be observed in the static DIT investigation (see Fig. 11). As indicated by Eq. (5), the DIT signal is proportional to the change in convective heat

transfer between thermograms. For a LSB, the change linked to the transition process is generally much stronger than the one associated with separation, which facilitates the detection of unsteady transition using DIT.

To illustrate the performance of the DIT technique for increasing pitch rates, DIT curves are constructed, centered at $\alpha = 2°$, using a 1-degree pitch difference between thermograms for various k. As the pitch rate increases, the time difference between thermograms needs to be decreased to maintain the pitch difference value constant. DIT curves, obtained during pitch up for four different reduced frequencies, are shown in Fig. 18 left, while the results obtained during pitch down are shown in Fig. 18 right.

The pitch up curves show a negative DIT peak associated with the unsteady transition location, visible for every frequency. This location is always downstream of the static value (in agreement with surface pressure measurements and PIV), with the difference increasing with frequency as expected. The strength of the DIT peak generally decreases with increasing frequency, as the physical time between DIT frames reduces. However, no clear positive peak is visible upstream of transition, expected to indicate the unsteady separation location, with the possible exception of the lowest value of k. Similarly, measurement noise downstream of transition obscures the proper identification of the reattachment location. A different behavior is observed during pitch down. Now, unsteady transition appears as a positive DIT peak, caused by the change in direction of the bubble. This feature could only be detected for small motion frequencies, but does appear upstream of the static location. The obtained results suggest that DIT performs better during pitch up, which can be explained when considering that in the transition region, the flow changes from laminar to turbulent along the pitch up motion, thus enhancing surface cooling
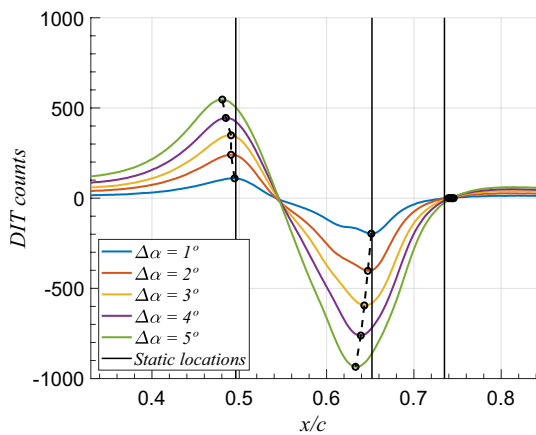

Fig. 17 DIT curves at $\alpha = 2°$ for the thermally quasi-steady pitching wing, using various separations between infrared frames, $\Delta\alpha$
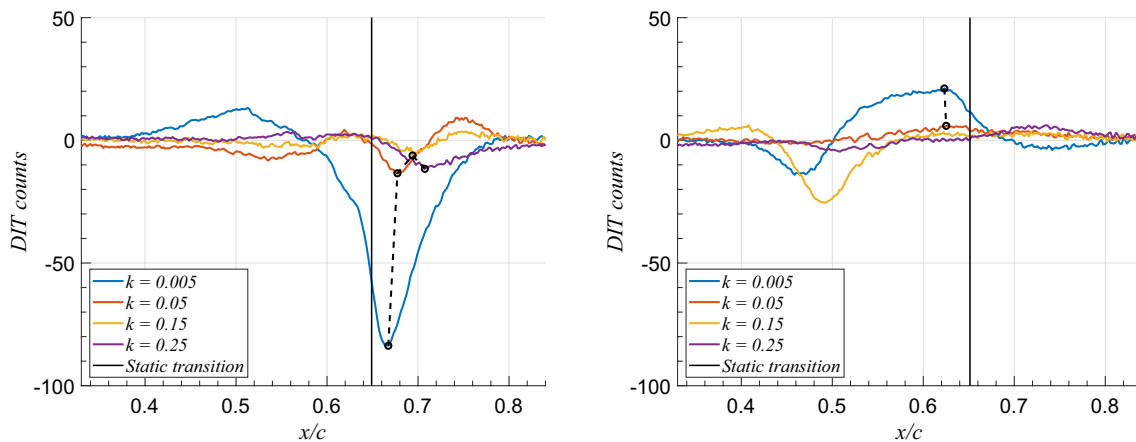

Fig. 18 DIT curves for the pitching wing at $\alpha = 2°$, for various motion reduced frequencies and using a separation between thermograms of one degree, during pitch up (left) and pitch down (right)

through convection. According to Eq. (5), DIT benefits from an initially warmer surface.

The results obtained with DIT for every reduced frequency tested, over the full range of pitch angles, are included in Fig. 19. The pitch up curves show transition downstream of the static value at the same incidence (extracted from the quasi-steady motion, $k = 0.0002$), with the deviation increasing with higher level of unsteadiness, which is in agreement with previous studies (see, for example, Pascazio et al. (1996) or Lee and Basu (1998)). The results during pitch down are inconclusive, being similar for every motion frequency investigated.

Despite the difficulties with the determination of the characteristic LSB locations in unsteady flow situations, a main advantage of the infrared approach is that it may provide insight into the three-dimensional behavior of the flow along the span of the wing. Even though this property is of no particular relevance for the present study, where the thermographic measurements are analyzed in a spanwise-averaged manner to reduce the measurement noise, an example of a DIT distribution along the span is shown in Fig. 20. This distribution was obtained during pitch up at a reduced frequency of $k = 0.05$. It shows a negative signal, linked to the unsteady transition process, revealing that the unsteady transition front is spanwise uniform, as it was also observed in the case of steady inflow.

3.3 LSB hysteresis analysis

The LSB hysteresis is analyzed based on the phase-averaged c_p distributions. This is done by comparing the characteristic locations measured at $\alpha = 2°$ as a function of pitch rate, considering all quasi-steady and unsteady cases listed in Table 1, as shown in Fig. 21. The results indicate that the hysteresis in bubble location increases as the reduced
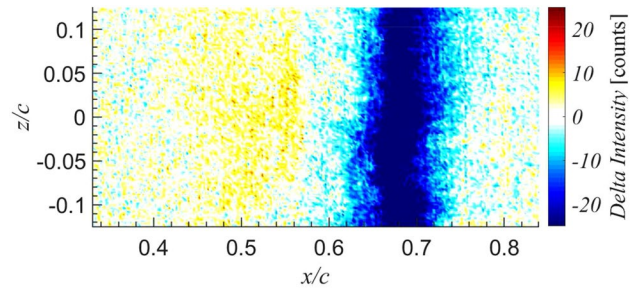

Fig. 20 Example of a DIT distribution obtained for a pitch up case and $k = 0.05$

frequency of the motion is raised, which is most clearly visible from the unsteady transition location. For unsteady separation, the results seem to be affected by the discretization effect of the pressure taps, whereas little information could be obtained for unsteady reattachment during pitch up due to the bubble being too far downstream.

The surface pressure measurements also allow to perform an analysis of the aerodynamic hysteresis in terms of the circulation around the airfoil through lift coefficient (c_ℓ) estimations. For the experiments, the instantaneous lift coefficient during the pitching motion can be obtained from numerical integration of the phase-averaged c_p distributions. It should be noted that the fabrication process did not allow placing a pressure tap at the trailing edge. For integration purposes, interpolation is necessary in that region, for which the static pressure at the trailing edge is estimated to be the mean between the measurements from the suction and pressure sides of the wing closest to that point. The unsteady lift coefficient obtained for the pitch up and pitch down motions is shown in Fig. 22 left for $k = 0.05$ and in Fig. 22 right for $k = 0.15$, where the experimental results are compared to the static inviscid slope (2π) and the prediction of a model based
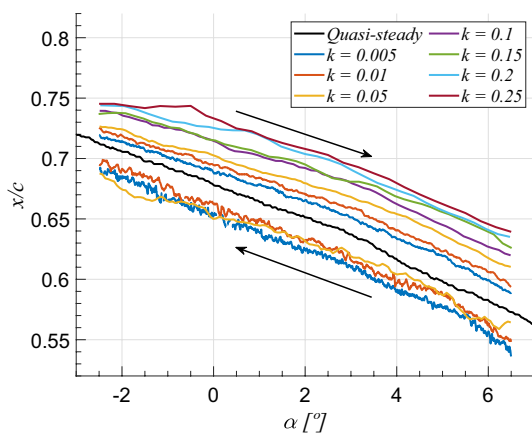

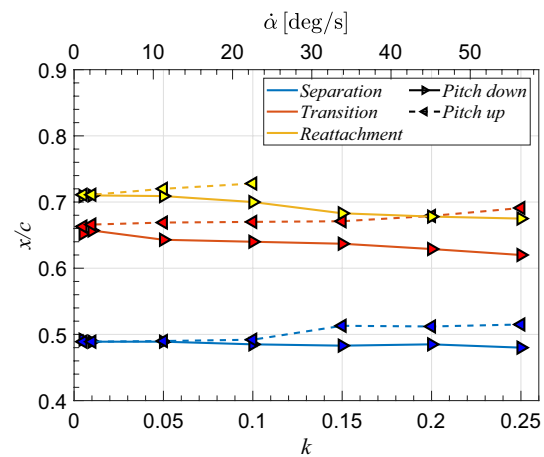**Fig. 19** Unsteady transition location for the pitching wing, obtained from DIT for every reduced frequency tested

Fig. 21 LSB characteristic locations estimated from c_p distributions, for various levels of aerodynamic unsteadiness, with $\alpha = 2°$
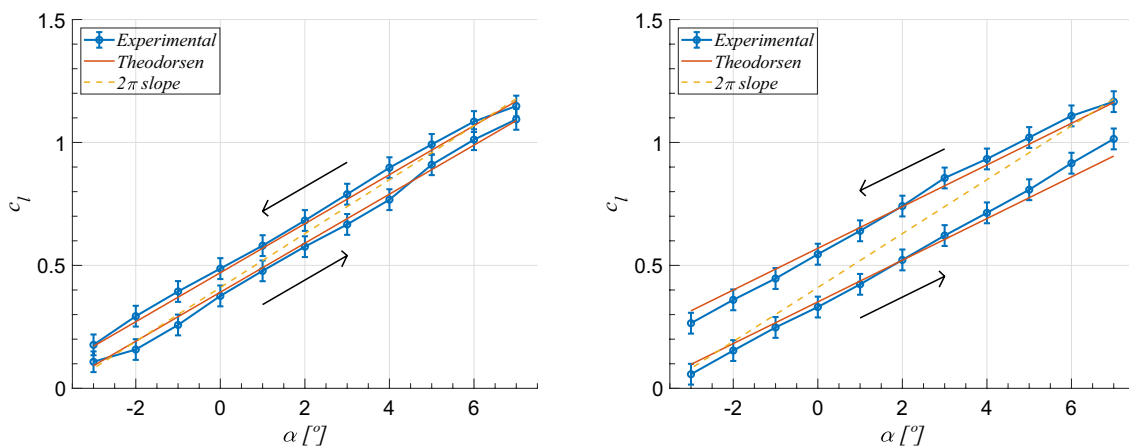
Fig. 22 Unsteady lift coefficient for the pitching wing, with $k = 0.05$ (left) and $k = 0.15$ (right)

on Theodorsen's theory that was adapted to the considered motion with a constant pitching rate (Leishman, 2006). In this model, the circulatory response behaves similarly to that of a pure angle of attack change, where lift shows a phase lag with respect to α. This means that the unsteady lift is lower than its corresponding static value for increasing incidence, while the opposite occurs for decreasing incidence. The amplitude of the response is adapted by including the constant pitching rate term, which may be expressed as:

$$c_\ell = \pi \frac{c}{2} \left[\frac{\dot{\alpha}}{U_\infty} \right] + 2\pi C(k) \left[\alpha + \frac{c}{2} \left(\frac{1}{2} - a \right) \frac{\dot{\alpha}}{U_\infty} \right], \qquad (7)$$

where the only contributions are those caused by the change in angle of attack and the constant pitching rate. Here, C is Theodorsen's function and $a = -0.2$ due to the wing pitching axis located at 40% of the chord.

The unsteady lift coefficient, which is proportional to the circulation around the wing, is linked to the unsteady behavior of the LSB in the following. The considered approach for this analysis consists of comparing the transition hysteresis of the LSB between pitch up and pitch down, at a constant angle of attack and at a constant value of the instantaneous lift coefficient, c_ℓ, both based on the measurements with the pressure sensors. The angle of attack that is chosen for this analysis is $\alpha = 2°$ and the corresponding lift coefficient is equal to that of the static wing at this α, which is $c_\ell(\alpha = 2°) = 0.63$. This comparison of the LSB hysteresis in transition location with respect to a constant pitch angle and a constant lift coefficient is shown in Fig. 23. While both situations indicate a nearly linear increase in hysteresis with the level of aerodynamic unsteadiness imposed, the results at a constant lift coefficient are approximately 50% lower. This suggests that the effect of the unsteady pressure gradient on the bubble location is approximately twice as large as the effect on the change in circulation around the wing.
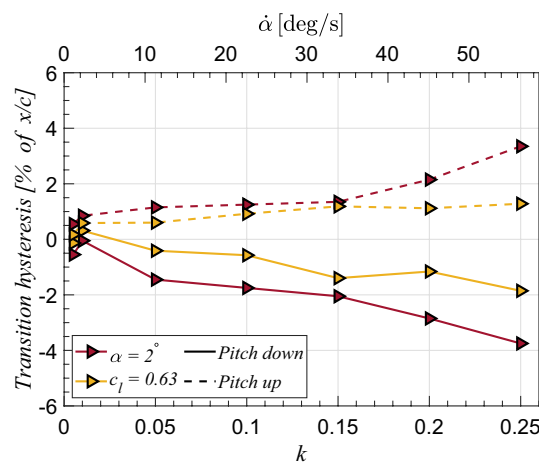

Fig. 23 Comparison of the hysteresis in transition location extracted from surface pressure distributions, between the case at a constant pitch angle of $\alpha = 2°$ and at a constant lift coefficient of $c_\ell = 0.63$

4 Assessment of the experimental techniques

The results presented in the previous section have shown that the three considered measurement techniques (surface pressure measurements, PIV and IT/DIT) can all be used to determine the characteristic locations of steady and unsteady LSBs. However, specific limitations apply to the respective techniques that are discussed in detail in this section, leading to an holistic assessment of the suitability of the three techniques for aerodynamic wind tunnel testing that involves the characterization of LSBs.

For steady flow conditions, it is observed in Fig. 12 that the detection of all three LSB features generally works well for the three different experimental techniques. A limitation of the surface pressure measurements is the missing data for

the reattachment location near the trailing edge, which is caused by the limited spatial resolution of the pressure taps. The PIV-based results show the complete LSB behavior over the entire considered range of incidence angles; however, problems were encountered with the automated detection and extrapolation of the dividing streamline upstream of the LSB. This results in an increased uncertainty of the separation point, which is evident by the relatively large differences to the other two techniques for this characteristic, compared to transition and reattachment. The steady LSB characterization results based on the infrared thermography measurements on the other hand show no clear limitations, as they are generally consistent and overall in good agreement with the other two techniques.

The limitations of the surface pressure measurements and the PIV-based approach that were described for the steady test cases remain unaffected by the introduction of unsteady flow conditions. It should, however, be noted that PIV measurements were conducted for only two reduced frequencies, due to relatively large experimental efforts associated with the flow field measurements. In contrast, the detection of the LSB characteristics based on the infrared measurements with DIT is heavily affected for the unsteady test cases where the pitch rate of the wing is increased above the thermally quasi-steady range. A quantification of this effect is given by performing a comparison between the three techniques in terms of the measured hysteresis in transition location. The hysteresis is typically defined as the difference between the pitch up and pitch down case; however, only limited reliable information could be obtained from pitch down using DIT. To overcome this limitation, hysteresis is alternatively defined here relative to the static transition location. A positive (negative) value means that the unsteady transition location occurs downstream (upstream) of the static one. The obtained results are shown in Fig. 24, for the wing at $\alpha = 2°$, as a function of the reduced frequency and the corresponding pitch rate. The surface pressure and PIV measurements (where available) agree quite well and suggest that hysteresis is approximately symmetric between pitch up and pitch down. Instead, the hysteresis measured with DIT (for pitch up) increases rapidly before reaching a linear evolution that shows a consistently higher value than the other two techniques (approximately 3% of the chord higher). This behavior is analogous to that measured by Wolf et al. (2019) for a sinusoidally pitching airfoil at a higher Reynolds number. As discussed by Richter et al. (2016), who compared DIT with hot-film sensors and pressure transducers, this additional hysteresis is argued to be caused by the thermal lag of the model surface.

The discussed limitations of the three different experimental techniques in terms of their capability to characterize LSBs can be used to evaluate the suitability of the techniques for aerodynamic wind tunnel testing of steady and
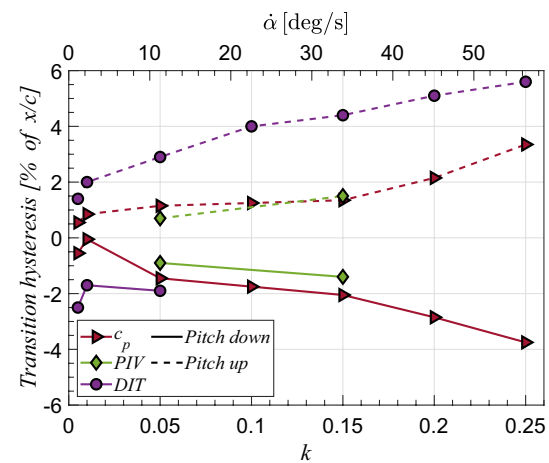

Fig. 24 Hysteresis in transition location obtained for the unsteady wing with respect to the static value, for $\alpha = 2°$ and every reduced frequency tested

unsteady LSBs. For that, it is important to also consider the experimental effort and the inherent advantages of each measurement technique. Such an overview of the strengths and weaknesses of the three techniques is given in Table 4. Each of the measurement techniques has a distinctive advantage over the others: for the pressure measurements that is the additional availability of load estimations, for PIV that is the quantitative flow field information and for infrared thermography that is the availability of information along the spanwise direction. It follows that no general recommendation can be given for any particular technique; instead the ideal technique or combination of techniques depends on the specific application and the quantities of interest. For the investigation of the transition hysteresis with respect to the lift that was performed in this study, the surface pressure measurements were the only suitable technique. However, as a different example, DIT can be considered as the preferred technique for a study of the spanwise behavior of an LSB on swept wings or more complex three-dimensional wing geometries, where the quantitative value for the LSB hysteresis is known from a different technique or of no direct interest, such as in Mertens et al. (2022).

5 Conclusion

The steady and unsteady behavior of a laminar separation bubble has been studied in a series of wind tunnel experiments. The presence and nature of the bubble were analyzed through the identification of the characteristic locations that define this flow feature: the separation of the laminar boundary layer, the transition to turbulence in the separated shear layer and the subsequent reattachment of the turbulent shear layer. Three different techniques have been used to identify

Table 4 Qualitative assessment of the three experimental techniques

Measurement technique	Advantages	Disadvantages
Surface Pressure	Information about airfoil loads Commonly available in WT models	Low spatial resolution Model instrumentation required Possible boundary layer interference
PIV	LSB flow topology High temporal resolution No model instrumentation	Missing data near the surface Relatively high experimental effort
Infrared Thermography	Spanwise measurement data Relatively low experimental effort No model instrumentation	Dependence on surface properties Typically low temporal response

these characteristic locations, viz. surface pressure measurements, particle image velocimetry and infrared thermography, with the objective of assessing their respective advantages and limitations.

The LSB was first characterized under static conditions, over a range of angles of attack, with one-degree increments, between $-3° \leq \alpha \leq 7°$. The LSB was for the first time also characterized using an extension of the differential infrared thermography method, establishing the proof of concept of this technique for detecting all three characteristics of the LSB. Then, a pitching-type motion, of the form $\alpha = 2° \pm 5°$, was applied to the wind tunnel model to study the effect of the unsteady pressure gradient on the nature and location of the LSB. The surface pressure measurements provided the opportunity to compare the hysteresis in bubble location to that of circulation, by analyzing the bubble movement at a constant lift coefficient. This was obtained from numerical integration of phase-averaged surface pressure distributions, showing good agreement with linear unsteady theory predictions (Theodorsen). The comparison was made upon the hysteresis in transition location with respect to the static value, showing a nearly linear increase with the level of aerodynamic unsteadiness imposed. While this holds both for constant pitch rate or constant lift conditions, the latter showed significantly lower levels (approximately 50%). It is argued that the unsteady pressure gradient causes an additional effect on the location of the LSB, apart from a change in circulation, thus increasing the hysteresis between the pitch up and pitch down parts of the motion.

For steady flow conditions, the assessment of the performance of the experimental techniques, based on a comparison of the LSB characterization results, revealed that the infrared measurements deliver better results than the other two techniques, with both exhibiting some measurement artifacts. When considering the results obtained from the measurements during the pitching motion of the wing, the surface pressure measurements and PIV were not severely affected by the change in experimental conditions. Instead, the infrared method became limited by the thermal response of the aerodynamic surface, meaning that none of the three techniques could be identified

as generally best suited for this application. It was found that the DIT technique could only detect the effects of the unsteady transition process when applied in thermally unsteady conditions. Furthermore, the hysteresis in transition location measured with DIT is higher than the one measured with the pressure taps or PIV, which is argued to be caused by the additional thermal lag of the surface. This behavior is in agreement with previous research on the use of DIT for unsteady transition detection. A simplified thermal model suggests that the DIT signal is governed by the non-dimensional group Fo Bi. As a design guideline for future experiments, it is therefore recommended to select materials with a lower thermal capacity and/or increase the level of convective heat transfer by adapting the wind tunnel model to run at higher velocities, while increasing the levels of external irradiation accordingly.

Declarations

References

Balzer W, Fasel HF (2016) Numerical investigation of the role of free-stream turbulence in boundary-layer separation. J Fluid Mech 801:289–321. https://doi.org/10.1017/jfm.2016.424

Bergh H, Tijdeman H (1965) Theoretical and experimental results for the dynamic response of pressure measuring systems. Tech. Rep. NLR-TR F.238, Nationaal lucht-en ruimtevaartlaboratorium, Amsterdam, Netherlands

Borgmann D, Hosseinverdi S, Little J et al (2020) Investigation of low-speed boundary-layer instability and transition using experiments, theory and DNS. AIAA Aviati Forum. https://doi.org/10.2514/6.2020-2948

Boutilier MS, Yarusevych S (2012) Parametric study of separation and transition characteristics over an airfoil at low Reynolds numbers. Exp Fluids 52(6):1491–1506. https://doi.org/10.1007/s00348-012-1270-z

Burgmann S, Schröder W (2008) Investigation of the vortex induced unsteadiness of a separation bubble via time-resolved and scanning PIV measurements. Exp Fluids 45(4):675–691. https://doi.org/10.1007/s00348-008-0548-7

Dollinger C, Balaresque N, Sorg M et al (2018) IR thermographic visualization of flow separation in applications with low thermal contrast. Infrared Phys Technol 88:254–264. https://doi.org/10.1016/j.infrared.2017.12.001

Dovgal AV, Kozlov VV, Michalke A (1994) Laminar boundary layer separation: instability and associated phenomena. Prog Aerosp Sci 30(1):61–94. https://doi.org/10.1016/0376-0421(94)90003-5

Ericsson LE, Reding JP (1988) Fluid mechanics of dynamic stall part I. Unsteady flow concepts. J Fluids Struct 2(1):1–33. https://doi.org/10.1016/S0889-9746(88)90116-8

Gardner A, Weiss A, Heineck J et al (2020) (2021) Boundary layer transition measured by DIT on the PSP rotor in forward flight. J Am Helicopter Soc 022008:1–10. https://doi.org/10.4050/jahs.66.022008

Gardner AD, Eder C, Wolf CC et al (2017) Analysis of differential infrared thermography for boundary layer transition detection. Exp Fluids 58(9):1–14. https://doi.org/10.1007/s00348-017-2405-z

Gartenberg E, Roberts AS (1991) Airfoil transition and separation studies using an infrared imaging system. J Aircr 28(4):225–230. https://doi.org/10.2514/3.46016

Gaster M (1967) The structure and behaviour of laminar separation bubbles. Aeronaut Res Counc Rep Memo 3595:1–31

Gerakopulos R, Boutilier MSH, Yarusevych S (2010) Aerodynamic characterization of a NACA 0018 airfoil at low reynolds numbers. In: 40th AIAA Fluid Dynamics Conference and Exhibit. pp 1–13. https://doi.org/10.2514/6.2010-4629

Ghorbanishohrat F, Johnson D (2018) Evaluating airfoil behaviour such as laminar separation bubbles with visualization and IR thermography methods. In: J Phys: Conf Ser PAPER 1037. https://doi.org/10.1088/1742-6596/1037/5/052037

Giguère P, Selig MS (1997) Low reynolds number airfoils for small horizontal axis wind turbines. Wind Eng 21(6):367–380

Grawunder M, Ress R, Breitsamter C (2016) Thermographic transition detection for low-speed wind-tunnel experiments. AIAA J 54(6):2012–2016. https://doi.org/10.2514/1.J054490

Guerra AG, Hosseinverdi S, Sing A et al (2021) Unsteady evolution of a laminar separation bubble subjected to structural motion. AIAA Aviat Aeronaut Forum Expos, AIAA Avitation Forum 2021:1–18. https://doi.org/10.2514/6.2021-2949

Guerra AG, Hosseinverdi S, Little J et al (2022) Unsteady behavior of a laminar separation bubble subjected to wing structural motion. AIAA Sci Technol Forum Expos, AIAA SciTech Forum 2022:1–17. https://doi.org/10.2514/6.2022-2331

Guissart A, Romblad J, Nemitz T et al (2021) Small-scale atmospheric turbulence and its impact on laminar-to-turbulent transition. AIAA J 59(9):3611–3621. https://doi.org/10.2514/1.J060068

Hodson HP, Howell RJ (2005) Bladerow interactions, transition, and high-lift aerofoils in low-pressure turbines. Annu Rev Fluid Mech 37:71–98. https://doi.org/10.1146/annurev.fluid.37.061903.175511

Horton H (1968) Laminar separation bubbles in two and three dimensional incompressible flow. PhD thesis, University of London

Hosseinverdi S, Fasel HF (2019) Numerical investigation of laminar-turbulent transition in laminar separation bubbles: the effect of free-stream turbulence. J Fluid Mech 858:714–759. https://doi.org/10.1017/jfm.2018.809

Kim DH, Chang JW (2010) Unsteady boundary layer for a pitching airfoil at low Reynolds numbers. J Mech Sci Technol 24(1):429–440. https://doi.org/10.1007/s12206-009-1105-x

Kurelek JW, Kotsonis M, Yarusevych S (2018) Transition in a separation bubble under tonal and broadband acoustic excitation. J Fluid Mech 853:1–36. https://doi.org/10.1017/jfm.2018.546

Kurelek JW, Tuna BA, Yarusevych S et al (2020) Three-dimensional development of coherent structures in a two-dimensional laminar separation bubble. AIAA J 59(2):1–13. https://doi.org/10.2514/1.j059700

Lang M, Rist U, Wagner S (2004) Investigations on controlled transition development in a laminar separation bubble by means of LDA and PIV. Exp Fluids 36(1):43–52. https://doi.org/10.1007/s00348-003-0625-x

Lee T, Basu S (1998) Measurement of unsteady boundary layer developed on an oscillating airfoil using multiple hot-film sensors. Exp Fluids 25:108–117. https://doi.org/10.1007/s003480050214

Leishman JG (2006) Principles of helicopter aerodynamics, 2nd edn. Cambridge University Press, Cambridge

Mertens C, Wolf CC, Gardner AD et al (2020) Advanced infrared thermography data analysis for unsteady boundary layer transition detection. Meas Sci Technol 31(1):015301. https://doi.org/10.1088/1361-6501/ab3ae2

Mertens C, Grille Guerra A, van Oudheusden BW, et al (2022) Analysis of the boundary layer on a highly flexible wing based on infrared thermography measurements. In: 23. DGLR/STAB Symposium, Berlin

Michelis T, Yarusevych S, Kotsonis M (2017) Response of a laminar separation bubble to impulsive forcing. J Fluid Mech 820:633–666. https://doi.org/10.1017/jfm.2017.217

Miozzi M, Capone A, Costantini M et al (2019) Skin friction and coherent structures within a laminar separation bubble. Exp Fluids 60(1):1–25. https://doi.org/10.1007/s00348-018-2651-8

Moffat RJ (1988) Describing the uncertainties in experimental results. Exp Therm Fluid Sci 1(1):3–17. https://doi.org/10.1016/0894-1777(88)90043-X

Mueller TJ, DeLaurier JD (2003) Aerodynamics of small vehicles. Annu Rev Fluid Mech 35:89–111. https://doi.org/10.1146/annurev.fluid.35.101101.161102

Nati A, de Kat R, Scarano F et al (2015) Dynamic pitching effect on a laminar separation bubble. Exp Fluids 56(9):1–17. https://doi.org/10.1007/s00348-015-2031-6

O'Meara MM, Mueller TJ (1986) Experimental determination of the laminar separation bubble characteristics of an airfoil at

low Reynolds numbers. AIAA Pap. https://doi.org/10.2514/6.1986-1065

Pascazio M, Autric JM, Favier D, et al (1996) Unsteady boundary-layer measurement on oscillating airfoils: transition and separation phenomena in pitching motion. In: 34th Aerosp Sci Meet Exhib https://doi.org/10.2514/6.1996-35

Raffel M, Merz CB (2014) Differential infrared thermography for unsteady boundary-layer transition measurements. AIAA J 52(9):2090–2093. https://doi.org/10.2514/1.J053235

Reeh AD, Tropea C (2015) Behaviour of a natural laminar flow aerofoil in flight through atmospheric turbulence. J Fluid Mech 767:394–429. https://doi.org/10.1017/jfm.2015.49

Ricci R, Montelpare S (2005) A quantitative IR thermographic method to study the laminar separation bubble phenomenon. Int J Therm Sci 44:709–719. https://doi.org/10.1016/j.ijthermalsci.2005.02.013

Richter K, Wolf CC, Gardner AD, et al (2016) Detection of unsteady boundary layer transition using three experimental methods. In: 54th AIAA Aerosp Sci Meet 0(January):1–22. https://doi.org/10.2514/6.2016-1072

Rudmin D, Benaissa A, Poirel D (2013) Detection of laminar flow separation and transition on a NACA-0012 airfoil using surface hot-films. J Fluids Eng, Trans ASME 135(10):1–6. https://doi.org/10.1115/1.4024807

Simon B, Filius A, Tropea C et al (2016) IR thermography for dynamic detection of laminar - turbulent transition. Exp Fluids 57(5):1–12. https://doi.org/10.1007/s00348-016-2178-9

Spalart PR, Strelets MK (2000) Mechanisms of transition and heat transfer in a separation bubble. J Fluid Mech 403:329–349. https://doi.org/10.1017/S0022112099007077

Toppings CE, Yarusevych S (2021) Structure and dynamics of a laminar separation bubble near a wing tip. J Fluid Mech. https://doi.org/10.1017/jfm.2021.881

Visbal MR, Gordnier RE, Galbraith MC (2009) High-fidelity simulations of moving and flexible airfoils at low Reynolds numbers. Exp Fluids 46(5):903–922. https://doi.org/10.1007/s00348-009-0635-4

von Hoesslin S, Stadlbauer M, Gruendmayer J et al (2017) Temperature decline thermography for laminar-turbulent transition detection in aerodynamics. Exp Fluids 58(9):1–10. https://doi.org/10.1007/s00348-017-2411-1

von Hoesslin S, Gruendmayer J, Zeisberger A et al (2020) Visualization of laminar-turbulent transition on rotating turbine blades. Exp Fluids 61(6):1–10. https://doi.org/10.1007/s00348-020-02985-9

Watmuff JH (1999) Evolution of a wave packet into vortex loops in a laminar separation bubble. J Fluid Mech 397:119–169. https://doi.org/10.1017/S0022112099006138

White FM (2006) Viscous fluid flow, 3rd edn. McGraw-Hill Book Company, New York

Wieneke B (2017) PIV Uncertainty Quantification and Beyond. PhD thesis, TU Delft University, https://doi.org/10.13140/RG.2.2.26244.42886

Wolf CC, Mertens C, Gardner AD et al (2019) Optimization of differential infrared thermography for unsteady boundary layer transition measurement. Exp Fluids 60(1):1–13. https://doi.org/10.1007/s00348-018-2667-0

Wolf CC, Gardner AD, Raffel M (2020) Infrared thermography for boundary layer transition measurements. Meas Sci Technol 31(11):112002. https://doi.org/10.1088/1361-6501/aba070

Wynnychuk DW, Yarusevych S (2020) Characterization of laminar separation bubbles using infrared thermography. AIAA J 58(7):2831–2843. https://doi.org/10.2514/1.J059160

Yarusevych S, Sullivan PE, Kawall JG (2009) On vortex shedding from an airfoil in low-Reynolds-number flows. J Fluid Mech 632:245–271. https://doi.org/10.1017/S0022112009007058